Performance of two innovative stress sensors imbedded in mortar joints of new masonry elements

Lidia La Mendola* [(1)], Maria Concetta Oddo [(1)], Maurizio Papia [(1)], Francesco Pappalardo [(2)], Agatino Pennisi [(2)], Gabriele Bertagnoli [(3)], Fabio Di Trapani[(3)], Alessia Monaco [(4)], Fulvio Parisi [(5)], Simone Barile [(6)]

[(1)] Engineering Department, University of Palermo, Italy
[(2)] STMicroelectronics S.r.l., System Research and Application, Catania, Italy
[(3)] Department of Structural, Geotechnical and Building Engineering, Politecnico di Torino, Turin, Italy
[(4)] Department of Architecture and Design, Politecnico di Torino, Turin, Italy
[(5)] Department of Structures for Engineering and Architecture, University of Naples Federico II, Naples, Italy
[(6)] Mapei S.p.A., Milan, Italy

* corresponding Author

Abstract

Many historical cities enjoy the presence of masonry buildings with inestimable historical, artistic and cultural value. Old masonry buildings often suffer structural deficiencies, design faults and materials aging process. In recent years, many researchers focused their attention on the opportunities that structural health monitoring (SHM) can ensure for the health state of existing masonry structures, where damages can be difficult to predict promptly and can cause brittle collapses with high risks for the community.

This paper presents an experimental study on the effectiveness of two stress sensor types for non-seismic SHM of new masonry elements. A ceramic sensor, based on piezoelectric principles, and a capacitive sensor were installed in mortar joints of two series of specimens made of calcarenite stone masonry and clay brick masonry. All specimens were tested under uniaxial compression with displacement control, to assess the effectiveness of sensors in recording pressures within different types of masonry for SHM applications under variation of load conditions. Even though both the ceramic and capacitive sensors were designed as stress sensors for concrete structures, their installation within mortar joints provided a good response, based on the comparison against more classical measurement devices. Results demonstrate the suitability of the sensors even for SHM of masonry structures.

Keywords: structural health monitoring; masonry walls; piezoelectric stress sensors; capacitive stress sensors; experimental testing.

1. Introduction

In the last decades, the advent of smart sensing technology has motivated the scientific community to emphasise the need for near-real-time performance and safety monitoring systems for both new and existing constructions. Special attention has been focused on existing built heritage because of its natural and gradual deterioration that, in most cases, calls for a constant and effective control of safety levels and operating conditions over the time.

Both calamitous events and natural aging processes have pointed out that an adequate diagnostic system is essential to detect structural changes that could affect the performance and safety of a structure [1-3].

A constant monitoring system can be useful to identify damage onset and propagation to support decision making and keep safety above target levels. Moreover, the possibility to implement monitoring systems also in new masonry constructions is another highly relevant issue for development of 'smart structures' in urban areas. This innovative idea applied over a large territorial scale can produce the advantage to control and significantly increase safety of strategic buildings, which many times have masonry structure, especially in historic towns.

Structural health monitoring (SHM) is defined as a process that allows collecting big data sets on real performance of structures, either to develop analytical models for structural assessment or to activate early warning systems in case performance thresholds are exceeded during strong events. It can now be deployed on large scale to infrastructures as a standard option (even since construction) and not only when specific pathologies are found [4-6].

During the last decade, the evolution of low-cost sensors derived from TLC industry, the development of high-speed internet communication, the birth of cloud-based services and the rise of big data platforms able to apply artificial intelligence techniques, have changed the possible scenario of structural monitoring. Different types of SHM systems have been developed such as contactless sensors with high-resolution cameras, drones and contact robotic sensors [7]. Those monitoring systems are well known and used in the fields of automotive and aerospace engineering. Conversely, SHM systems have been rarely used in structural and infrastructure engineering for a long time, due to their instrumentation cost, ability to ensure long-term monitoring, and complexity of the installation process.

To make an evocative example, the current Airbus A350 model has a total of close to 6000 sensors across the entire plane and generates 2.5 Tb of data per day, while the newer model, launched in 2020, captures more than three times that amount [8]. Aircraft Sensors Market was worth USD 1.68 billion in 2017 and is projected to reach USD 2.36 billion by 2023 [9]. On the other hand, almost no civil engineering structure is nowadays designed and built with a standard supply of sensors in it like planes and cars, but living within non monitored structures is not yet felt as a lack of safety by common opinion.

In recent years, several researchers focused their attention on a new and low-cost generation of sensors based on Micro Electro-Mechanical Systems (MEMS) technology. These sensors work with micro-movements of micrometric mechanical systems that are read via electronic effects. The state of the art on MEMS includes sensors such as inclinometers, accelerometers and magnetometers. In detail, high-accuracy, low-power, two-axis digital inclinometer with ultra-low noise density enables high-resolution tilt sensing as well as sensing of low-level, low-frequency vibration, as required in structural health monitoring. Accurate inclination and vibration measurements can support the condition-based safety assessment of structures (e.g., buildings and tall towers) and infrastructure (e.g., bridges and tunnels). Affordable, battery-powered MEMS tilt sensors enable many more structures to be monitored for safety than has been economically viable using earlier, more expensive technologies [10]. On top of MEMS technology, novel stress sensors based on piezoresistive or capacitive technologies delineate an emerging category of monitoring systems. Piezoresistive stress sensors with ceramic package have been already used inside concrete structures, whereas capacitive stress sensors are available only as prototype and they are constantly improving under several experimentations. The state of the art enhances the optimization of the sensors' layout for health monitoring of new structures by incorporating a sensor network that has been already designed [4]. The problem complexity increases when the installation of SHM systems in existing masonry structures is considered, as shown for instance in [12-15], but this issue is outside the scope of this study.

This paper presents two innovative monitoring systems for new masonry buildings based on piezoresistive and capacitive, low-cost, stress sensors. The installation of capacitive stress sensors embedded in mortar joints of masonry is proposed and their effectiveness is evaluated through experimental testing. The piezoresistive stress sensor is located inside a ceramic package and works with the deformation of piezoresistive elements arranged upon a ceramic plate under strain force. The resistive value of the piezoresistive element changes during the deformation phase, so the former is closely related to the strain. The capacitive sensor consists of two conductive plates with a thin dielectric foil between them. The capacitive value, which is measured in terms of picofarads (pF), changes with the variation of distance between the plates under strain force. An experimental campaign was conducted on calcarenite and clay brick masonry panels, allowing a detailed assessment of the sensors' response to loads. Given that masonry buildings can suffer progressive and extensive damage under gravity loads and other loading actions, the proposed sensors were investigated by testing 12 masonry panels under compressive loading. This allowed the sensors to detect stress variations within the masonry. Then, data recorded by sensors was compared to that provided by traditional measuring devices. Moreover, experimental results are also compared to analytical estimates according to current code provisions and a macroscopic constitutive model available in the literature.

2. Brief history of research on proposed ceramic sensor

In 2015, some authors of this paper began to develop a ceramic (piezoresistive) stress sensor, which was the subject of a patent [16]. These studies were further developed and industrialised in collaboration with STMicroelectronics, leading to a second patent [17] and production of the first device prototypes in 2016. That sensor is a ceramic disc with the dimensions of a coin (Figure 1a) and it is made of three Aluminum Oxide (Al_2O_3) layers with thickness of approximately 1.5, 0.5 and 1.5 mm, respectively. The central layer is glued to the external ones by means of two layers of glass frit bonding with a thickness between 10 μm and 50 μm.

Several ruthenium oxide piezo-resistances are placed inside the intermediate ceramic layer within oriented cuts and trenches in order to measure the deformation of the sensor in different directions, either separately or in combination. Two Wheatstone bridges shown in Figure 1b are realized on the upper face of the intermediate ceramic layer and embedded inside the top glass frit. The first bridge is called 'planar' as it is supposed to be affected only by the strains laying in the plane of the sensor, whereas the second bridge is called '3D' as it is supposed to be affected by the complete strain state within the sensor.

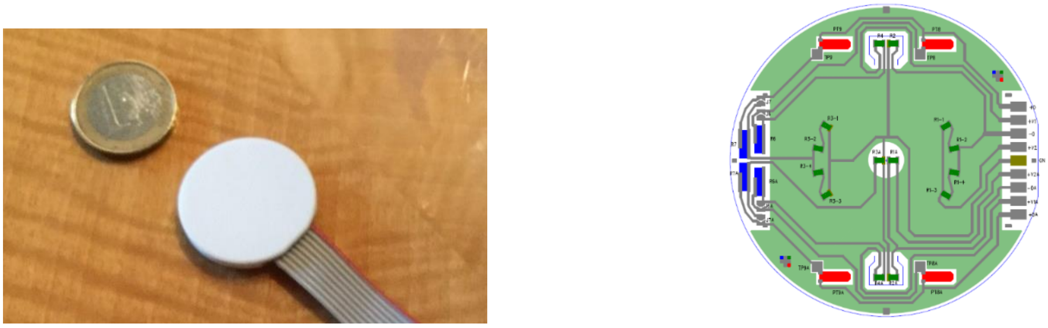

(a) (b)

Figure 1. Ceramic stress sensor: (a) overall view; (b) electrical scheme of Wheatstone bridges.

Since ceramic is a perfectly elastic material, a direct calculation of the stress in a given direction is possible is the field of the typical stress rates of concrete. The working principle of the device is the possibility to measure the force acting on its round surfaces, and therefore the average pressure orthogonal to those surfaces, without any direct measure of concrete deformation.

The sensor was designed to be embedded inside a concrete casting tied to the reinforcement cage, and its application within concrete structures under short-term loading has been presented in [18]. A second experimental campaign was performed to investigate the behaviour of the sensor under long-term loading [19], therefore facing time-dependent properties of concrete.

The effectiveness of this sensor to be applied within masonry mortar joints (i.e., calcarenite stones or clay bricks) is explored in the paper, providing also information about the installation modalities. A new capacitive stress sensor is also proposed in the paper for the same purposes. Details are illustrated in the following section.

3. Proposed capacitive stress sensor

The capacitive sensor presented in this paper (Figure 2) is based on a deep experience on strain force sensor for structural health monitoring. The first sensor, developed by STMicroelectronics between 2012 and 2015, was very small and based on piezoresistive effect of Complementary Metal Oxide Semiconductor (CMOS) transistors on silicon die. That preliminary study highlighted that the size of sensors for monitoring stresses in large structures plays a key role. Therefore, a further research effort was oriented towards the development of a capacitive sensor as a big sensing element directly faced to concrete or other construction materials, leading to a novel patent in 2019 [20].

The capacitive sensor discussed herein consists of a parallel-plate capacitor with Kapton as dielectric layer and in this case the sensitive element area is that of the full plate surface. Moreover, the area can be realized as big as needed to be comparable to the macro-characteristics of the construction elements (Figure 2a). Capacitive sensors have a diameter 40 mm of (Figure 2b) and a thickness of 1.65 mm, moreover vertical sensors can be equipped with two brackets (Figure 2c). The latter allow the sensors working also under tensile loading in addition to compression.

(a) (b) (c)

Figure 2. Capacitive sensor: (a) electrical scheme; (b) global view of horizontal sensors; (c) brackets of vertical sensor.

The capacitance, C, of a parallel plate capacitor is given by:

$$C = \frac{\varepsilon A}{d} \qquad (1)$$

where ε, A and d are the permittivity of the gap, the area of electrodes, and the gap between the electrodes, respectively. The dielectric used in the sensor is Kapton with dielectric constant value $\varepsilon_r = 3.4$.

The change in capacitance is proportional to the variation in strain according to the variation in the gap between the electrode plates, namely the distance between the plates. In Figure 3, capacitance-distance relationship in Eq. (1) is plotted by assuming $\varepsilon = \varepsilon_0 \cdot \varepsilon_r$ with vacuum dielectric constant $\varepsilon_0 = 8.8542 \cdot 10^{-3}$ pF/mm and $A = 346.36$ mm^2. It is important to highlight that, depending on the working range of sensor capacitance, the electrode distance variation will provide a different capacitance range, according to Eq. (1).

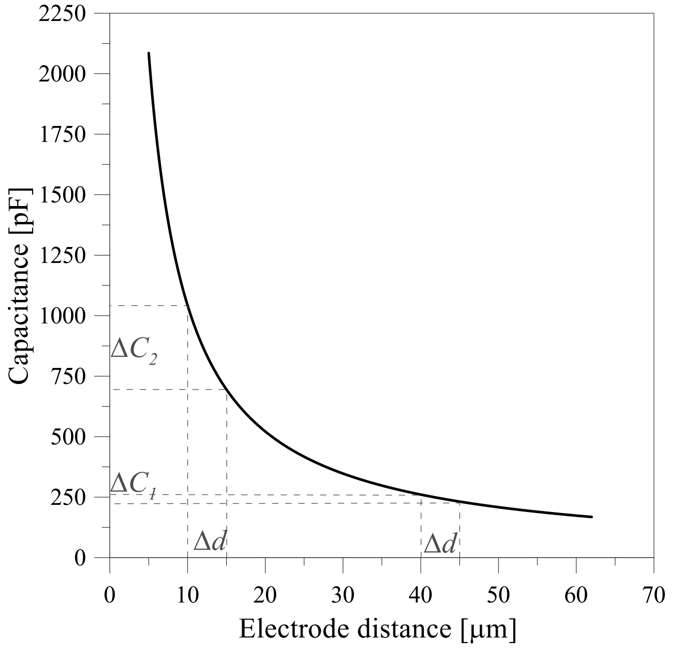

Figure 3. Capacitance versus electrode distance relationship.

Signal conditioning electronics converts the capacitance signal to voltage, current or frequency. The electronics is collocated close to sensing element to mitigate parasitic capacitance, but it is external to the sensor parts connected with the structure to be tested. The capacitive sensor offers advantages including high sensitivity, high stability and low temperature sensitivity.

4. Experimental investigation on masonry monitoring

The sensors presented in previous sections were inserted in masonry wall specimens to evaluate their effectiveness under compressive loading. In total, twelve specimens were manufactured and tested, six of them were made of calcarenite stone bricks coming from Sabucina quarry, close to Caltanissetta (Italy), and the other six specimens were made of solid clay bricks. Calcarenite bricks had the same standard size of clay bricks (250×120×50 mm^3), they were extracted from stones of usual dimensions coming from the quarry**.** Calcarenite stone and clay bricks have unit weight equal to 18.20 kN/m^3 and 17.00 kN/m^3, respectively. Compressive strengths of calcarenite stone and clay bricks were was obtained by experimental tests performed according to UNI EN 1926 [21] and UNI EN 772 [22], respectively. Monotonic compressive tests were carried out on six cubes of calcarenite stone (Figure 4a) and clay bricks (Figure 4b) with side of 100 and 50 mm, respectively. A 800 kN nominal load Zwick-Roell testing machine was used to perform the tests. Results listed in Table 1 showed an average compressive strength of 11.80 MPa and 23.39 MPa for calcarenite stone and clay bricks, respectively.

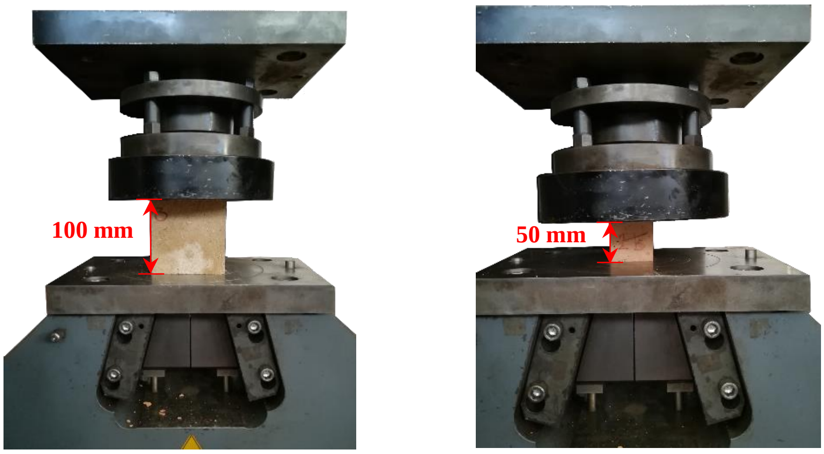

(a) (b)

Figure 4. Compressive tests: (a) calcarenite stone; (b) clay bricks.

Table 1. Compressive test results on calcarenite and clay bricks cubes.

Type	Specimen label	Maximum stress [MPa]	Average maximum stress [MPa]	COV [%]
CALCARENITE	C_1	15.20	11.80	20.27
	C_2	8.20		
	C_3	9.48		
	C_4	12.50		
	C_5	13.77		
	C_6	11.62		
CLAY BRICK	L_1	22.34	23.39	14.20
	L_2	23.97		
	L_3	28.73		
	L_4	26.10		
	L_5	19.97		
	L_6	19.24		

All specimens were fabricated with a premixed cementitious mortar having a M5 grade (f_m= 5 MPa), composed by 15% dosage of hydrated lime and cement and 85% of aggregates with grain size distribution between 0.1 mm and 1.4 mm, normally used for bedding bricks and concrete blocks.

After a curing period of 28 days (UNI EN 1015-11 [23]), the three-point bending tests (Figure 5a) on twelve 40×40×160 mm mortar prisms provided an average flexural strength of 2.23 MPa. Subsequently, from compressive on the twenty-four resulting mortar portions (Figure 5b) an average strength of 8.36 MPa (Table 2) was obtained.

(a) (b)

Figure 5. Test set up for mortar: (a) three point bending test; (b) compressive test.

Table 2. Average mechanical properties of mortar.

Mortar M5	**Average flexural strength [MPa]**	**Average compressive strength [MPa]**
	2.23	8.36
COV	(1.18%)	(5.88%)

The specimens were labelled as "SPn_m", where 'm' indicates the masonry type (i.e., C = calcarenite, L = clay bricks) and 'n' the number assigned to each sample. Table 3 reports details about sensor types and position in the joints with respect to the reference system x-y shown in Figure 5.

Table 3. Specimens and sensors (dimensions in mm).

ID sample	**Masonry type**	**Sensors Set-up**	**Capacitive stress sensors ID**		**Ceramic stress sensors ID**	
			x=195.0 y=185.0	x=315.0 y=185.0	x=195.0 y=185.0	x=315.0 y=185.0
SP1_C	Calcarenite	2 horizontal capacitive stress sensors	nZ4	nZ3	-	-
SP2_C			X5	X6	-	-
SP3_C		1 horizontal capacitive stress sensor + 1 horizontal ceramic stress sensor	-	nZ6	9_9H	-
SP4_C			-	X8	45_20H	-
SP5_C		2 horizontal ceramic stress sensors	-	-	41_29H	12_6H
SP6_C			-	-	44_26H	1_1H
SP1_L	Clay brick	2 horizontal capacitive stress sensors	nZ1	nZ2	-	-
SP2_L			X3	X4	-	-
SP3_L		1 horizontal capacitive stress sensor + 1 horizontal ceramic stress sensor	-	nZ5	50_32H	-
SP4_L			X7	X7	11_BH	-
SP5_L		2 horizontal ceramic stress sensors	-	-	2_2H	48_30H
SP6_L			-	-	10_AH	3_3H

Each specimen was composed of seven rows of either clay or calcarenite masonry units (250×120×50 mm) and interposed mortar joints having a thickness of 10 mm.

Capacitive and ceramic sensors were pre-installed in the panels during their manufacture, in the middle of the cross section, according to three patterns shown in Figure 6.

For both the masonry types, the following sensors were installed in the mortar bed joint close to the mid-height of each specimen, as shown in Figure 6: two capacitive stress sensors in SP1 and SP2 specimens; two ceramic stress sensors in SP5 and SP6 specimens; one ceramic and one capacitive stress sensor in SP3 and SP4 specimens. Moreover, in SP1, SP2, SP3 and SP4 specimens, an additional capacitive sensor with brackets was placed with vertically oriented plates into a vertical joint. Nonetheless, results of these latter sensors are not analysed below because the aim of the current paper is to assess the effectiveness of the proposed sensors in measuring compressive stresses within masonry.

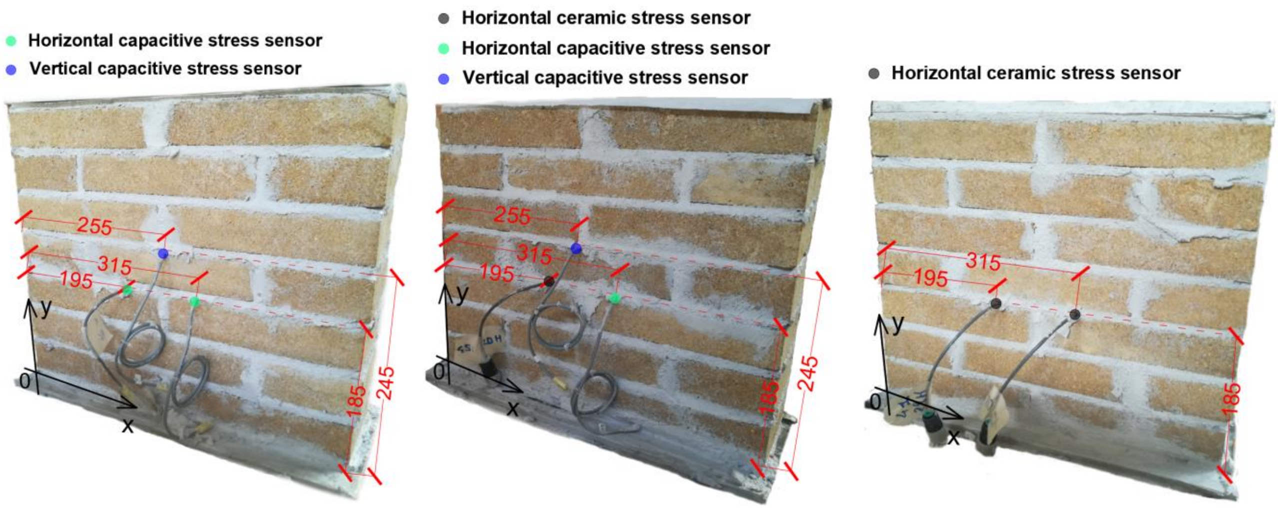

(a) (b) (c)

Figure 6. Monitoring patterns (dimensions in mm): (a) pattern with two horizontal capacitive sensors and an additional vertically oriented and placed in a vertical joint; (b) pattern with two horizontal stress sensors (one ceramic and one capacitive) and an additional capacitive sensor vertically oriented and placed in a vertical joint; (c) pattern with two horizontal ceramic sensors.

Figure 7 shows the installation of the sensors in the configurations above described, according to Table 3. The installation was a decisive and crucial phase as the main objective was to locate sensors correctly, avoiding any type of rotation and translation, during the installation operations. The use of a bubble level allowed checking that each row of bricks was exactly parallel to the support surface. That operation was required by the following reasons: (1) to guarantee the flatness of the sensors compared to the reference plane; and (2) to create a perfectly horizontal load surface in order to achieve a pure compression during the laboratory tests, avoiding any possible eccentricity. Any translation or rotation of the imbedded sensors was avoided by the fact that they were overwhelmed inside a layer of mortar and constrained in displacement by the weight of the brick located above them.

(a) (b) (c)

Figure 7. Installation of the sensors: (a) ceramic sensors in the mortar bed-joint; (b) capacitive sensor in vertical position; (c) capacitive sensors in the mortar bed-joint.

The ceramic and capacitive sensors, applied to the mortar bed joint considering their shape and geometry, were positioned without additional operations. The capacitive sensors installed in the vertical position provided to realize a 10 mm groove in the brick sides to embed the sensor brackets. Potential improvement of the sensor integration with the masonry could include an increased length of the brackets.

The masonry wall specimens so arranged were subjected to monotonic compressive loading, making the monitoring systems able to detect pressure variations in the masonry. Tests were performed through a Zwick-Roell testing machine having 4000 kN nominal load capacity and carried out in displacement control, adopting a displacement rate of 0.2 mm/min. Load data acquisition was performed by means of an integrated load cell. Two pre-loading cycles were performed in the range 20 - 100 kN to obtain a proper contact between the specimen and testing machine. This pre-load range was calibrated by means of a preliminary assessment of the compressive strength of the two types of masonry, as described in the next section. Two HEA200 steel beams with stiffening plates were placed at the bottom and on the top of each specimen to ensure a uniform load distribution. Variable Displacement Transducers (LVDTs) were glued on both sides, as depicted in Figure 8, to measure strains, Young's modulus, and to eventually recognize local phenomena.

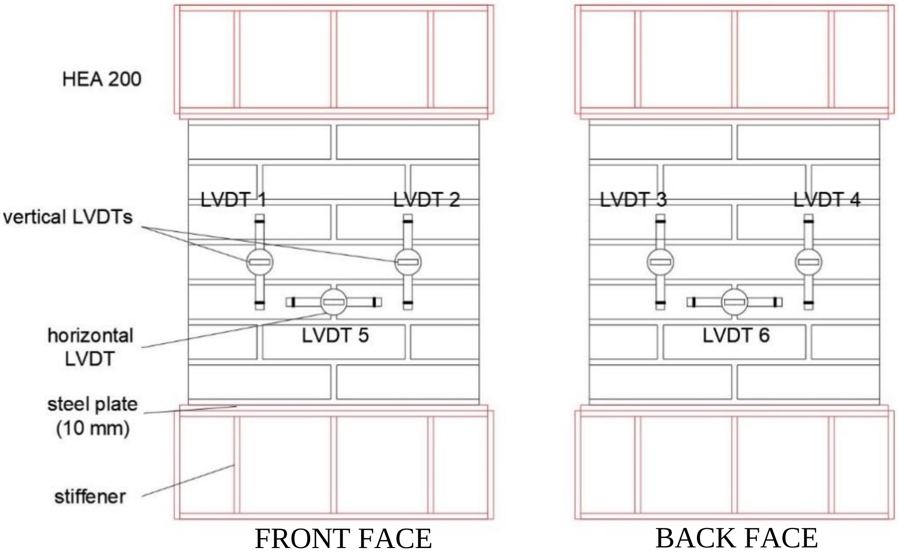

Figure 8. Traditional instrumentation for uniaxial compression tests.

5. Prediction of compressive response of masonry specimens

Both the design of the test set-up (in terms of expected maximum load, and choice of the acquisition system for the electronic signal by the sensors) and the validation of the experimental results were based on the analytical prediction of the mean values of the uniaxial compressive strength and Young's modulus of the masonry specimens. This prediction made use of the design equations provided in the Italian Technical Code [24, 25] for masonry structures to estimate average compressive strength and Young's modulus. In detail, Table 3 outlines the predicted values of mean compressive strength $f_{m,pred}$ and secant Young's modulus E_{pred} for calcarenite masonry and clay brick masonry. Such values were obtained through linear interpolation between tabular values associated with the characteristic compressive strength of the masonry units f_{bk} (i.e. calcarenite stones or clay bricks) and the mortar strength class M declared by the producer and defined by the mean compressive strength of mortar f_{mm}. The mortar used for the arrangement of the specimens was classified as M5 mortar, having $f_{mm} \geq 5$ MPa. Experimental tests on masonry unit specimens evidenced a mean compressive strength of 11.8 MPa for calcarenite stones and 23.4 MPa for clay bricks, with coefficients of variation equal to 20.3% and 14.2%, respectively. The Italian Technical Code allows calculating the characteristic compressive strength of masonry units as $f_{bk} = 0.75 f_{bm}$ for stones and $0.8 f_{bm}$ for clay bricks.

Therefore, the limits of the interpolation for prediction of the characteristic compressive strength of masonry were found to be the extreme values of the following ranges: 6 MPa ≤ f_k ≤ 7 MPa for clay brick masonry and 4.1 MPa ≤ f_k ≤ 4.7 MPa for calcarenite masonry. Thus, according to the code provisions, the mean compressive strength of masonry was obtained as $f_{m,pred}$ = 1.25f_k, whereas the Young's modulus was predicted as E_{pred} = 1000f_k. The predicted mechanical parameters of both calcarenite and clay brick masonries are reported in Table 4 and compared to their experimental counterparts $f_{m,exp}$ and E_{exp}. It is noteworthy to mention that the experimental values reported in Table 4 are the averages of all the compression tests of the two series of specimens (i.e., clay brick and calcarenite masonry panels). The experimental average values of Young's modulus were evaluated by using stress records from the load cell and displacement records by LVDTs.

Table 4. Comparison between experimental and code-based predicted mechanical parameters.

Masonry type	$f_{m,pred}$ [MPa]	E_{pred} [MPa]	$f_{m,exp}$ [MPa]	E_{exp} [MPa]	$f_{m,exp}/f_{m,pred}$	E_{exp}/E_{pred}
Calcarenite masonry	5.5	4424	7.36	6382	1.34	1.44
Clay brick masonry	8.4	6742	13.91	6378	1.65	0.95

The complete stress–strain behavior of the masonry panels can be predicted using some macroscopic constitutive models available in the literature. A comprehensive discussion about compressive stress–strain models and their impact on nonlinear behavior of masonry wall cross-sections under axial loading and bending moment is presented in [19]. Among the existing models, the empirical stress–strain equation proposed by Sargin in 1971 [26] for concrete members in compression, was adapted to calcarenite stone masonry in previous studies [27, 28]. That constitutive model considers masonry as a homogeneous material and is expressed by the following stress–strain relationship:

$$\tilde{\sigma} = \frac{A\tilde{\varepsilon} + (D-1)\tilde{\varepsilon}^2}{1 + (A-2)\tilde{\varepsilon} + D\tilde{\varepsilon}^2} \quad (2)$$

where: $\tilde{\sigma} = \frac{\sigma}{\sigma_0}$ and $\tilde{\varepsilon} = \frac{\varepsilon}{\varepsilon_0}$ are the ratios of the current axial stresses and strains to the peak stress σ_0 and corresponding strain value ε_0, respectively; A and D are parameters that need experimental calibration. As a matter of fact, the variation of A and D makes the model capable of being applied to many types of materials. Generally, in case of masonry, the range of variation that can be found for A is between 2 and 3, while D can vary between 0 and 2(A – 1). If the lower limit values of these parameters are assumed (i.e., A = 2 and D = 0), the stress–strain law of masonry denotes a brittle behavior. Conversely, if the upper limit values are chosen, then a relatively ductile compressive response is obtained. It is noteworthy that the parameter *A* influences the trend of the first branch of the stress–strain curve until peak stress because it defines the slope of tangent to the curve at the origin of the axes, calculated as the ratio between tangent and secant moduli $A = E_t/E_s$. The parameter *D* affects the ductility of the post-peak response in terms of absolute slope of the post-peak branch of the curve.

Cavaleri et al. [29] performed experimental tests on calcarenite masonry panels and they found that the best-fit values for *A* and D were respectively 2.8 and 1.2. The same values were assumed in this study to predict the theoretical compressive response of both the types of masonry. Figure 9 shows the comparison between experimental and analytical stress–strain curves, in which the peak stress values σ_0 are those listed in Table 4 (i.e., $f_{m,exp}$) and the corresponding ε_0 values are 0.0015 and 0.0055 respectively for calcarenite and clay brick masonry. The adopted values for *A* and *D* allow obtaining a theoretical prediction which falls in the range of the experimental results for both types of specimens, showing that the parameters originally calibrated for calcarenite stone masonry can be acceptable also for clay brick masonry. Details on the experimental results are reported in the following section. It is worth noting that a better calibration of the parameters *A* and *D* to define the stress–strain curves for both masonry types could be carried out, making a comparison with each single curve instead of the set of experimental points but this does not fall in the scope of this paper.

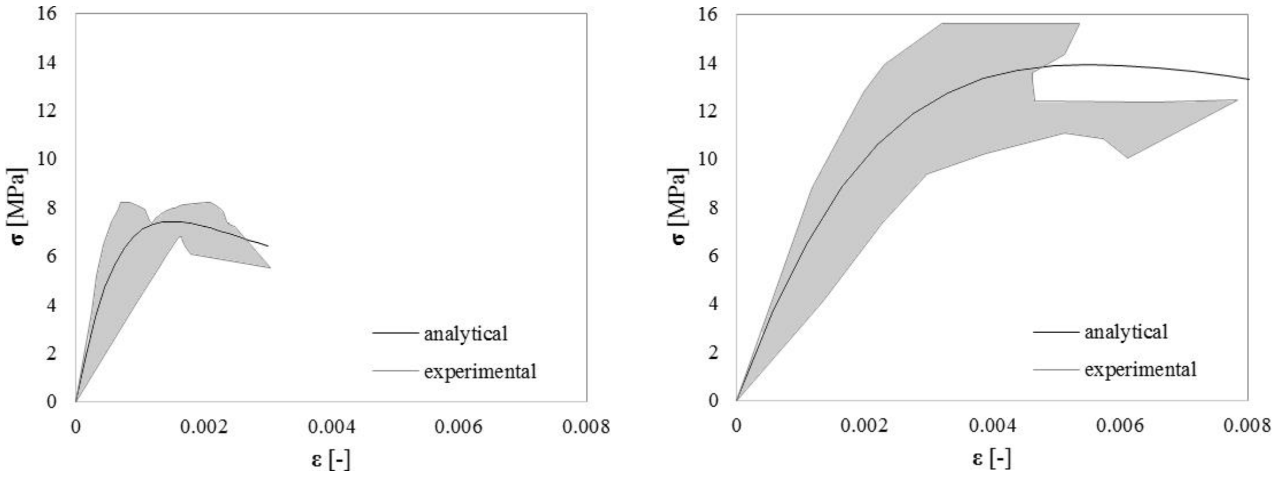

(a) (b)

Figure 9. Experimental results envelopes versus analytical stress–strain curves: (a) calcarenite masonry; (b) clay brick masonry.

6. Experimental results

Experimental data sets achieved from monotonic compression tests were post-processed in terms of stress–time curves for ceramic sensors and stress–capacitance with respect to the timeline for capacitive sensors. More in detail, the load data acquired by the load cell is simply divided by the cross-sectional area of the specimens (i.e., 510×120 mm^2) to get stresses. For the sensors (capacitive and ceramic) the recorded mechanical input is converted into an electric signal. This kind of transformation is performed by ceramic sensors thanks to their piezoresistive effect and by capacitive sensors thanks to their variability of capacitance with pressure. Ceramic sensors were calibrated during production, and it is recalled that they had been already validated by previous applications on concrete [18, 19], allowing the conversion of sensors readings into pressures. By contrast, capacitive sensor prototypes had not been calibrated yet, so raw sensor readings were directly expressed into pF units.

It should be noticed that all sensors measure a punctual value of the stress on an area of a few cm^2, which may locally differ from the average stress actually occurring in the masonry.

In this background, compressive tests provided data sets useful to calibrate the new capacitive stress sensor one the one hand, and to evaluate the effectiveness of the ceramic stress sensors for monitoring of masonry structures on the other hand.

6.1. Results from ceramic stress sensors

Figures. 10a-b and 8c-d show the experimental results for calcarenite brick masonry and clay brick masonry respectively, equipped with ceramic stress sensors (labelled as SP5_C, SP6_C, SP5_L, SP6_L). Results are compared in terms of stresses. Both ceramic stress sensors and machine load cell recorded a single data per second, so the two data sets are related to the same acquisition time. The comparison between the two measurement systems indicates similar data, with the same trend until the peak pressure. In the case tagged as 44_26H in Figure 10b, sensor reading curve assumed the trend of a noisy fluctuation. This behaviour was justified with a potential electromagnetic interference caused by the testing machine engine electromagnetic noise. In one case (SP5_L), the curves recorded by the ceramic stress sensors (2_2H and 48_30H in Figure 10c) diverged from the main trend, reaching out of range values, after that the peak stress was attained. This incongruency was most probably due to a local stress concentration or to potential damage to the sensor that occurred after that the maximum load was reached. However, although some damage can affect sensors results at high stress rates, it is noteworthy mentioning that their application for masonry SHM typically involves service loads.

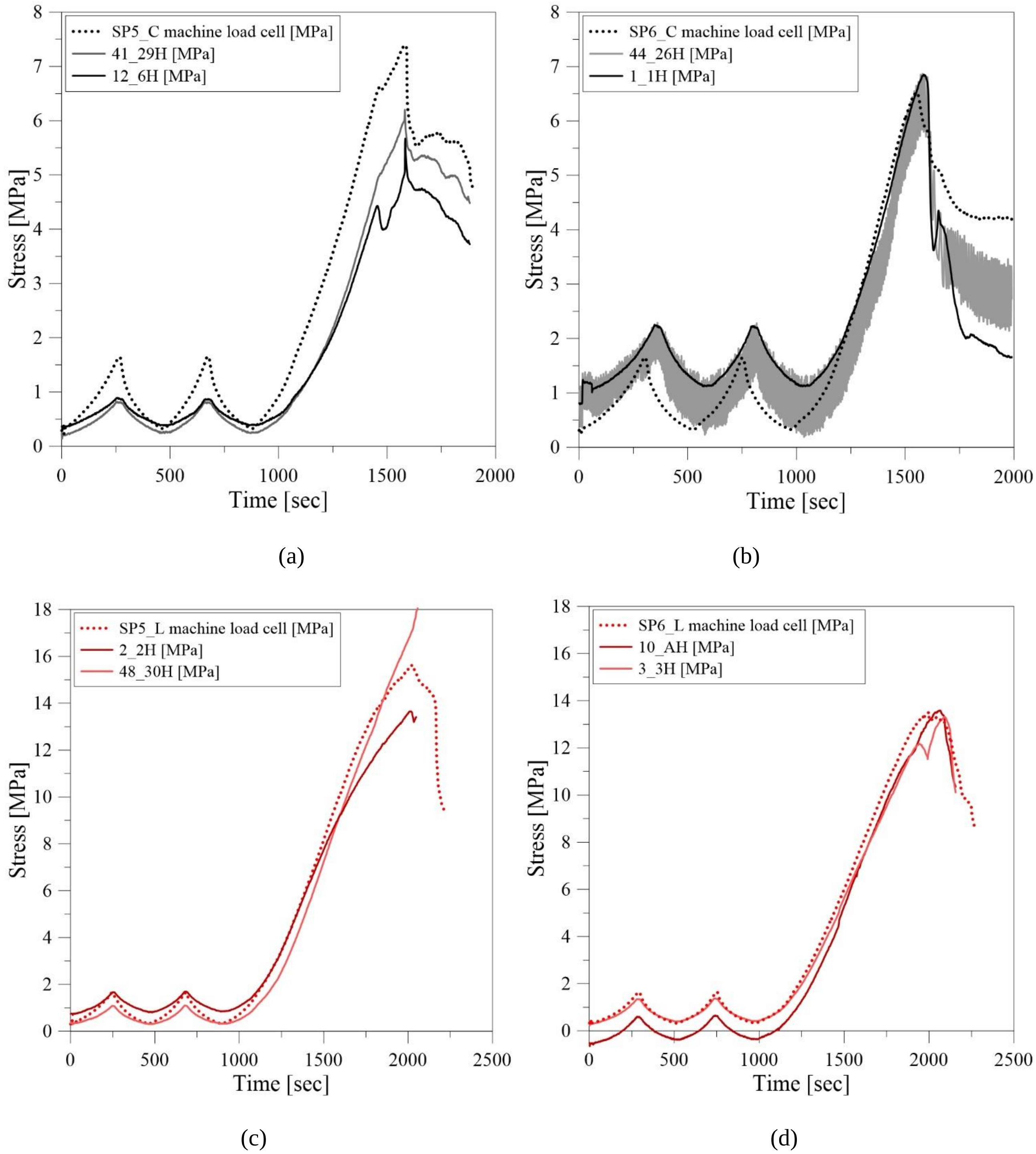

Figure 10. Comparison between ceramic stress sensor results and load cell data: (a), (b) calcarenite masonry; (c), (d) clay bricks masonry.

On average, the trend of the curves recorded by ceramic stress sensors reflected the observed evolution of load cell reference data. The sensors placed in specimen SP5_C seem to read a load weaker than the applied one, especially at low load levels (before 1000 sec). Better accordance is found on specimen SP6_C and on bricks masonry. Some electrical faults affected two sensors over eight, showing that robustness improvements are still needed.

Table 5 shows the values of compressive strength provided by ceramic stress sensors ($\sigma_{max,ceramic}$) compared to those recorded by the testing machine ($\sigma_{max,\mathbf{load\ cell}}$) in all the specimens equipped with these sensors, not only the ones presented in Figure 10. For ceramic stress sensor 48_30H, imbedded in specimen SP5_L, the value of $\sigma_{max,ceramic}$ is not reported because data recorded in the proximity of the peak load diverges from the reference trend towards unreliable values (Figure 10c).

Table 5. Recorded compressive strengths of specimens.

Specimen	$\sigma_{max,\mathbf{load\ cell}}$ [MPa]	$\sigma_{max,\ load\ cell}$ Avg. / STD [MPa]	$\sigma_{max,ceramic}$ [MPa]	$\sigma_{max,\ ceramic}$ Avg. / STD [MPa]	$\frac{\sigma_{max,ceramic}}{\sigma_{max,load.cell}}$
SP3_C	6.96	7.01 / 0.37	5.94	6.38 / 1.32	0.85
SP4_C	7.19		6.74		0.94
SP5_C	7.39		6.20 5.67		0.84 0.77
SP6_C	6.52		6.87 6.85		1.05 1.05
SP3_L	12.46	13.8 / 0.51	14.47	13.48 / 0.74	1.16
SP4_L	13.62		12.42		0.91
SP5_L	15.63		13.62 *		0.87 -
SP6_L	13.50		13.59		1.01 0.99

*data considered unrealistic.

Table 5 and Figure 11 include all results related to ceramic sensors, i.e. those related to sensors SP5_C, SP6_C, SP5_L, and SP6_L presented before and also those discussed in the following, inserted in specimens SP3_C, SP4_C, SP3_L, and SP4_L. Figure 11a summarizes the ratios between compressive strength recorded by ceramic stress sensors ($\sigma_{max,ceramic}$) and reference compressive strength ($\sigma_{max,load\ cell}$), highlighting a limited scattering of results with an average underestimation of 15% and 7.7% and an average overestimation of 5% and 8.4% for calcarenite and brick masonry specimens, respectively. Light stress overestimation is expected in these devices as ceramic is stiffer than mortar or masonry and therefore tends to concentrate the stress over the sensor. Comparison between average peak stress measures by the sensors and by the load cell are also shown in Figure 11b, which also shows the standard deviation bars. The latter confirm that the average measurements by sensors are really close to the average measures by the load cell. Further, results dispersion by the two measurement systems is in the same order of magnitude.

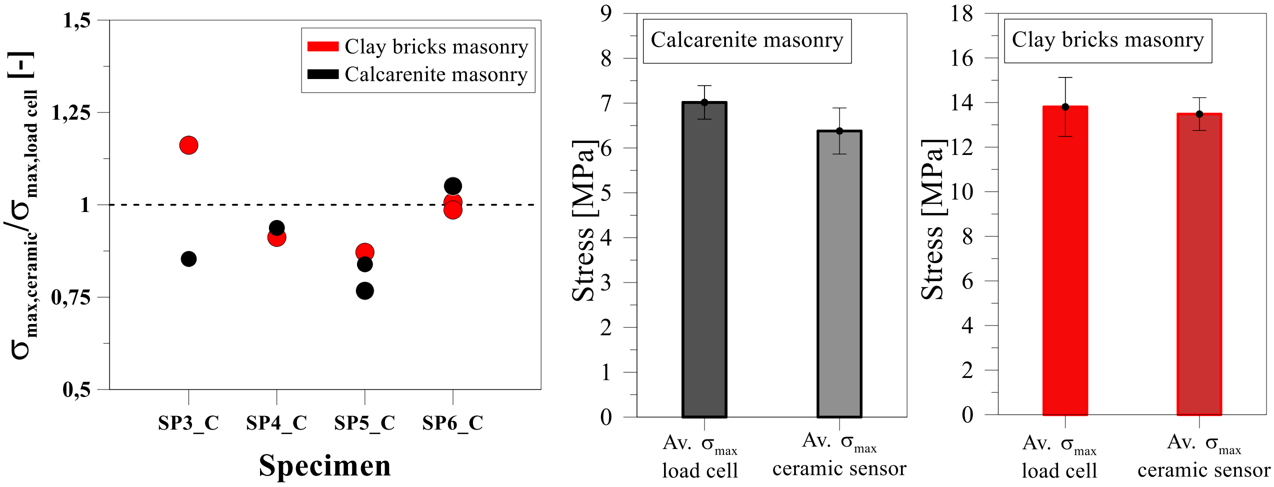

a) b) c)

Figure 11. Comparison between reference compressive strengths and maximum stresses recorded by ceramic stress sensors for calcarenite and clay brick masonry specimens: a) individual measures ratios; b) average and standard deviations for calcarenite masonry specimens; c) average and standard deviations for clay brick masonry.

6.2. Results of innovative stress capacitive sensors

Figures 12a-b and 12c-d show results for calcarenite and clay brick masonry equipped with capacitive stress sensors (SP1_C, SP2_C, SP1_L, SP2_L). Experimental data are plotted against two vertical axes, namely, one axis of pressure for data recorded by the machine load cell and the other axis of capacitance for data recorded by capacitive stress sensors. Sampling frequency of these latter data was 2 Hz (i.e., two times of that used for ceramic sensors). Nonetheless, in this study, the comparison between the two measurements is set in one data per second to ensure consistency with previous comparisons related to ceramic sensors. Some results from capacitive stress sensors showed a stepped shape due to the acquisition system resolution limit. Besides that, sensors were able to detect the global trend during the two pre-load cycles, the ascending loading branch, and peak compressive stress, sometimes recording also the post-peak behaviour (i.e., SP2_C and SP2_L). However, as previously remarked, data from capacitive stress sensors is not reported as pressure, because those sensors are still in a prototyping status and a consolidated transformation function from capacitance to stress is not yet available. Because of the same motivation, experimental plots start from different capacitance values: the capacity of each device at zero is different as the prototypes are hand-assembled. These sensors also follow the applied load with a different slope because, as shown in Figure 3, the trend of capacitance versus electrode distance relationship is nonlinear, implying that, for given Δd, the corresponding capacitance range ΔC varies in a significant way. More specifically, a linearization of ΔC should be made by means of a linear law with very different slopes depending as a function of the selected Δd range. The same Δd range implies low slopes for high values of *d* and high slopes for low values of *d*.

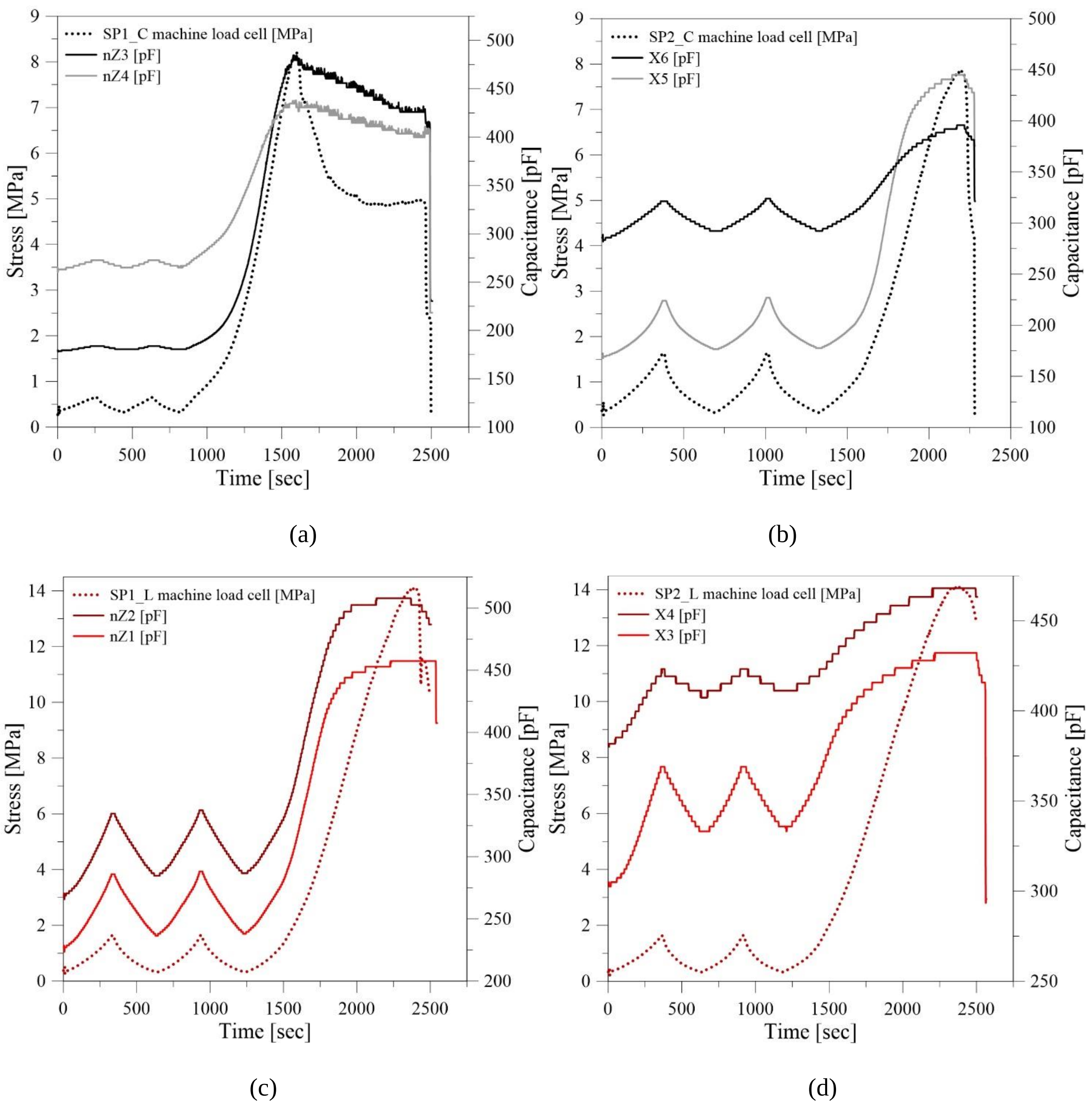

Figure 12. Comparison between capacitive stress sensor results and load cell data: (a), (b) calcarenite masonry; (c), (d) clay brick masonry.

Table 6 lists the values of maximum compressive strength ($\sigma_{max,load\ cell}$) and the corresponding maximum capacitance values in pF ($\sigma_{max,capacitive}$) recorded by capacitive stress sensors.

Table 6. Recorded compressive strength and capacitance values.

Specimen	$\sigma_{max,load\ cell}$ [MPa]	$\sigma_{max,capacitive}$ [pF]	
SP1_C	8.21	438.02	484.38
SP2_C	7.86	445.00	395.75
SP1_L	14.12	457.35	507.84
SP2_L	14.10	432.13	468.01

A correlation analysis was also performed by evaluating the Pearson's correlation coefficient [30-32] between stress and capacitance. Results are shown in Table 7, which demonstrates very high correlation exists between the two measures. Table 7 also outlines coefficients of correlation related to capacitive sensors presented in Section 6.3 for specimens SP3 and SP4.

Table 7. Pearson's correlation between pressure load and capacitance sensor readings.

Specimen	**ID capacitive stress sensor**	**Coeff. of correlation**
SP1_C	nZ4	0.971
	nZ3	0.968
SP2_C	X5	0.971
	X6	0.972
SP3_C	nZ6	0.982
SP4_C	X8	0.837
SP1_L	nZ1	0.942
	nZ2	0.939
SP2_L	X3	0.902
	X4	0.926
SP3_L	nZ5	0.920
SP4_L	X7	0.943

Currently, an in-depth capacitive sensors data analysis and characterization activities is ongoing, in order to defined an analytical relationship relating the capacitance (*C*) measured by the capacitive sensors and the applied pressure *p*, so that $p \simeq f(C)$. Anyway, the current tests gave the opportunity to study this relationship.

Figure 13 shows plots of the applied pressure versus the capacitive sensor measurements for SP1_C (Figures 13 a-b) and SP1_L (Figures 13 c-d) specimens, from the test beginning up to maximum load value.

For some sensors, the plots show that the pressure-capacitance relationship is quite linear, becoming distinctly nonlinear for other sensors. This may depend on many factors, such as sensor hand-assembling, installation flaws (even due to the sensors shape) potential heterogeneity of specimens (mortar joints and/or bricks). Further, since these sensors were designed to work well up to 8 MPa compressive stress, a better matching was found with calcarenite masonry specimens, characterized by a lower strengths. Conversely, lower accuracy was observed after 9 MPa stresses, as it can be observed in the case of clay brick masonry specimens. This evidence addresses further developments of the sensor toward a modification of the operative load range (i.e. by increasing the distance between the plates) in the case of masonries characterized by higher strength values.

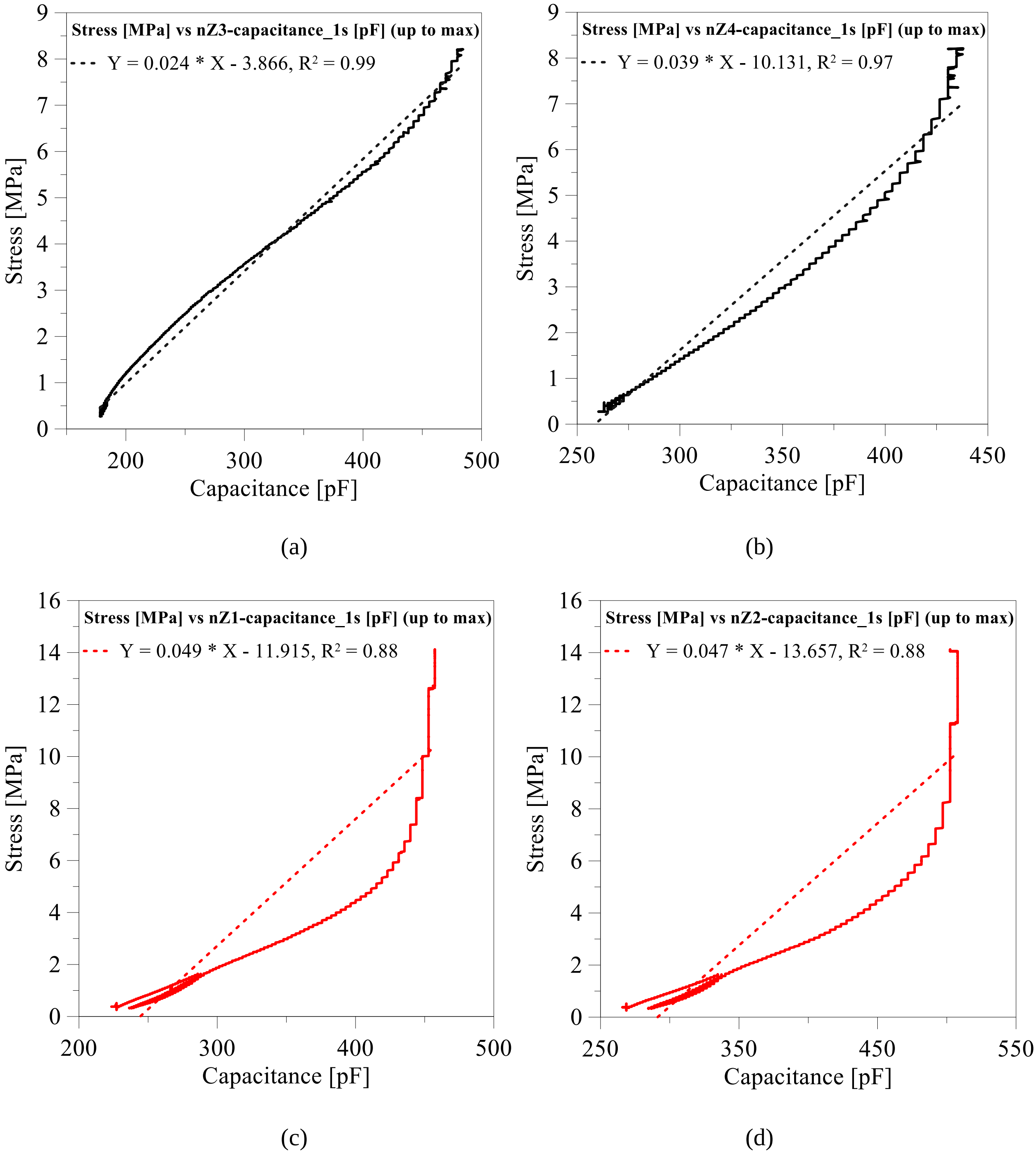

Figure 13. Pressure versus capacitance change in capacitive sensor measurements: (a), (b) calcarenite masonry; (c), (d) clay brick masonry.

Similar curves were obtained for SP2_C and SP2_L specimens, but they are not here reported for the sake of brevity. Due to the prototyping status of such a capacitive sensor, the obtained results do not allow a generalization of the relationships. Further investigations are ongoing to generalize, findings even with respect to different masonry typologies or concrete elements.

However, a comparative analysis of the sensor responses regardless of the scale of capacity in which they operate can be performed at the same way. To do this, a well know "min-max normalization" data processing technique [33], also known as "future scaling", is applied. Analytically this technique provides processing data by means of the following equation:

$$C_{norm} = \frac{C - C_{min}}{C_{max} - C_{min}} \quad (3)$$

where: C is the measured capacitance of each sensor and C_{min} and C_{max} are minimum and maximum values measured during the test, respectively. In this format, the curves related to the capacitive sensors records vary in the range [0,1]. Results are shown in Figures 14a and 14b, as an example for SP1_C and SP1_L specimens.

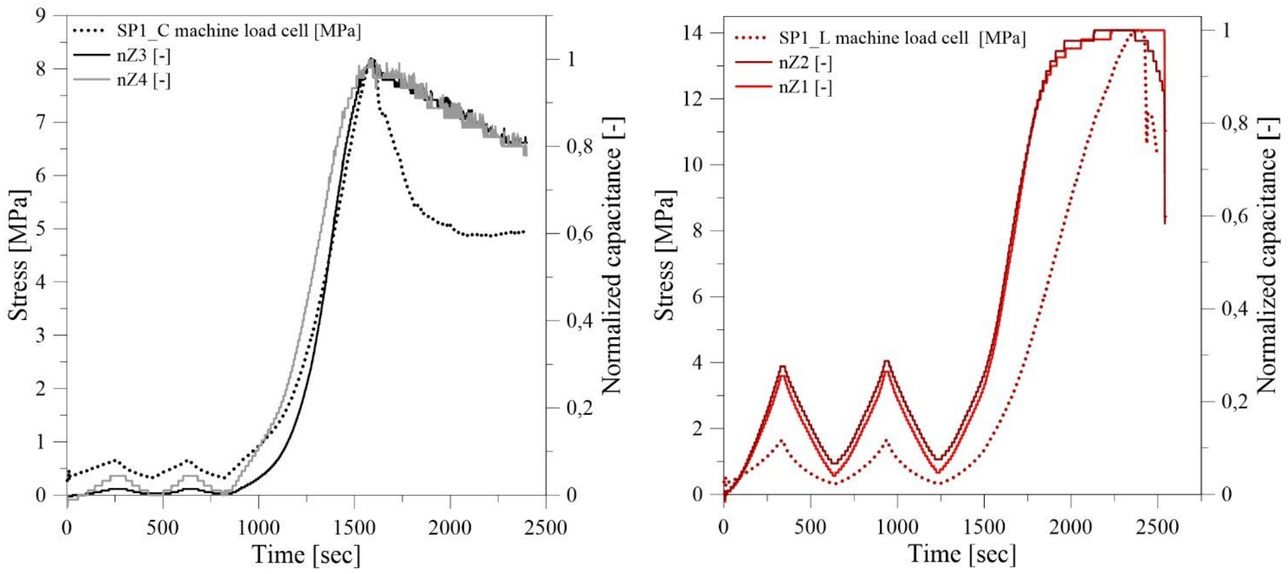

(a) (b)

Figure 14. Comparison between pressure and normalized capacitance: (a) calcarenite masonry (SP1_C); (b) clay brick masonry (SP1_L).

As shown in Figure 14, the trends of the normalized capacitance records from the sensors follow the mechanical stresses with a higher correlation both in the pre-load and peak-load phases.

6.3. Results from ceramic and capacitive stress sensors installed the same specimen

In the specimens SP3, ceramic and capacitive sensors are installed together. Figure 15 shows the comparison between stresses recorded by the machine load cell, stresses recorded by ceramic sensors and normalized capacitances obtained by capacitive sensors. It is worth noting that the three measurements have approximately the same trend over time.

In brick masonry, where higher loads are reached, ceramic sensors perform better than capacitive ones, because capacitive sensors suffer from overestimation of low load cycles (before 1200 sec) or overestimation of high loads (after 1700 sec) due to their nonlinear behaviour described before. Some nonlinearity of capacitive sensors can be also seen in calcarenite specimen SP4_C.

Nevertheless, results from experimental data post-processed until now, represent an important milestone and a starting point for future developments towards a more complete and detailed characterization of the capacitive stress sensor, moving forward on a complete family of capacitive sensors with different measurement ranges.

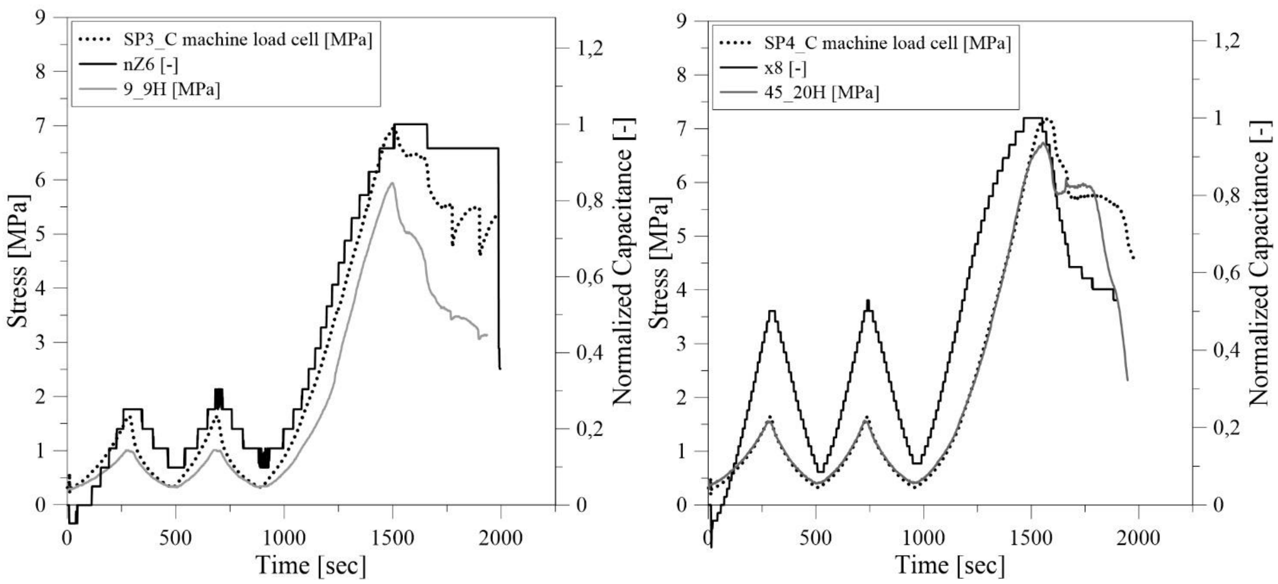

(a) (b)

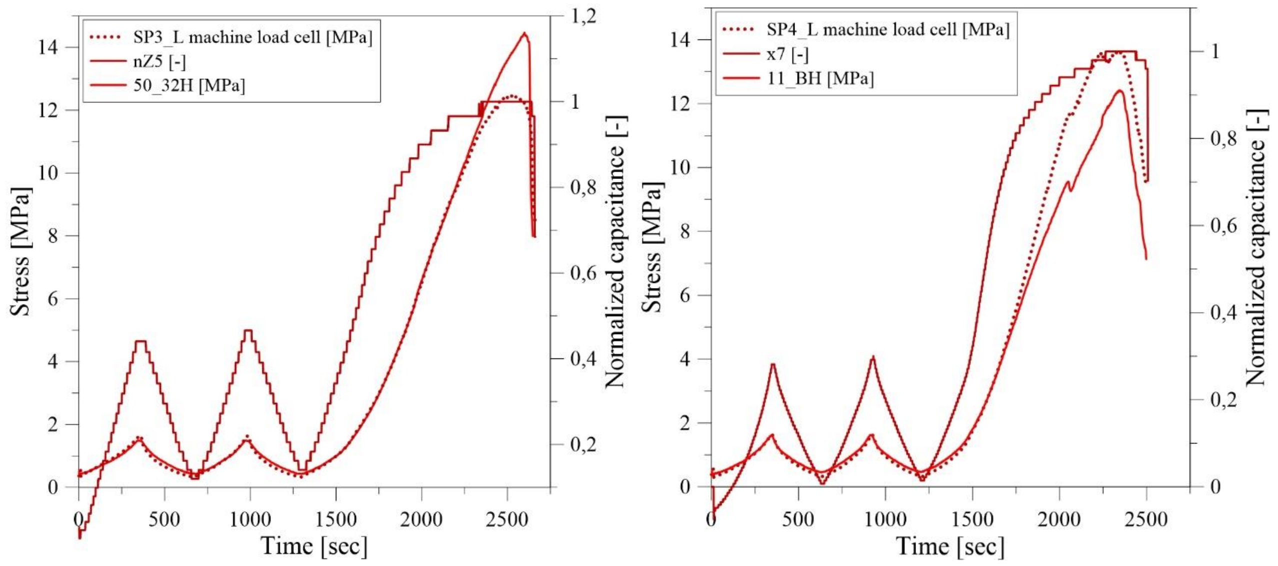

(c) (d)

Figure 15. Comparison between measurements of ceramic sensors, capacitive sensors and load cell data: (a), (b) calcarenite masonry; (c), (d) clay brick masonry.

7. Conclusions

This paper has presented the results of an experimental campaign related to the test of two stress sensors embedded inside masonry specimens, namely piezoelectric (ceramic) sensors and capacitive sensors. Both types of monitoring devices were designed to be embedded inside reinforced concrete structures, so their effectiveness for structural health monitoring of new masonry constructions was assessed in the paper.

Experimental tests were carried out on twelve masonry specimens, half of them were made of calcarenite bricks, the others by clay bricks. Compressive tests highlighted a highly nonlinear response of the masonries in the ascending branch, followed by a post-peak softening. Peak strength varied in the ranges 6.52÷8.21 MPa and 12.46÷15.63 MPa, for calcarenite and clay masonries, respectively.

Ceramic stress sensors showed very good agreement with the stresses recorded by the load cell. Results obtained from average peak stress comparisons were particularly favourable, in fact ceramic sensor peak stress averages underestimated by 10% in the case of calcarenite masonry and only by 3% in the case of clay brick masonry. Further, standard deviations by sensor readings were lower than 1 MPa, also showing a reduced results dispersion despite the heterogeneity of the supporting material and potential installation flaws. Because of this, a linear dependence was confirmed, without any need for any additional calibration with respect to that performed for the standard sensors already used for concrete structures. Results from capacitive sensors were compared in a more qualitative way, since their calibration is still ongoing. Sensor readings in terms of capacitance showed more pronounced correlation with recorded stresses in up to a threshold of 9 MPa. After, a highly nonlinear relationship was observed, and a full characterization is still ongoing to provide a stress/capacitance analytical relationship. It is noteworthy observing that the current tests of both the sensors were carried out up to the achievement of the peak load, although the application of these sensors for SHM purposes in most cases limit they operating range to service stresses. In this context the better results obtained in the lower stress ranges are encouraging. Overall, both the devices showed a positive response, demonstrating adequate potentialities to be implemented in SHM of new masonry structures and potentially also existing masonry structures. Research on the latter topic is of major interest and is still ongoing to complete the research program. The major challenges will address the effect of existing stress state on the masonry and the proper installation protocols for the sensors in an already built masonry wall.

Acknowledgements

This study was developed in the framework of PON INSIST (sistema di monitoraggio INtelligente per la SIcurezza delle infraSTrutture urbane) research project, which was funded by the Italian Ministry for Education, University and Research (Programma Operativo Nazionale "Ricerca e Innovazione 2014–2020", Grant No. ARS01_00913). The experimental tests were carried out in the Structures Laboratory of the University of Palermo and the support of the lab staff is gratefully acknowledged.

REFERENCES

[1] H. Sohn, C. R. Farrar, F. M. Hemez, D. D. Shunk, D. W. Stinemates, B. R. Nadler, J. J. Czarnecki, "A Review of Structural Health Monitoring Literature: 1996–2001" Los Alamos, NM: Los Alamos National Laboratories. 2004

[2] D. Balageas, C.-P. Fritzen, A. Güemes: "Structural Health Monitoring" Wiley, ISBN: 9781905209019, 2006.

[3] C. Boller, F.-K. Chang, Y. Fujino, "Encyclopedia of Structural Health Monitoring", Wiley, ISBN: 978-0-470-05822-0, 2009.

[4] C. R. Farrar, K. Worden, “Structural Health Monitoring, a Machine Learning Perspective”, John Wiley & Sons, ISBN: 978-1-119-99433-6, 2013.

[5] C. J. A. Tokognon, B. Gao, G. Y. Tian, Y. Yan, “Structural health monitoring framework based on internet of things: a survey”. IEEE Internet of Things J. vol.7(4), 2017.

[6] Dixit S, Sharma K. A review of studies in Structural Health Monitoring (SHM). Proc, Creative Construction Conference 2019, Budapest, Hungary.

[7] Sony S, Laventure S, Sadhu A. A literature review of next-generation smart sensing technology in structural health monitoring. Structural Control and Health Monitoring 2019; 26(3): e2321.

[8] B. Marr, “That’s data science: Airbus puts 10,000 sensors in every single wing!”, https://www.datasciencecentral.com/profiles/blogs/that-s-data-science-airbus-puts-10-000-sensors-in-every-single, 2015, last access 24/03/2019.

[9] “Aircraft Sensors Market Size, Share - Segmented by Sensor Type (Temperature, Pressure, Position, Flow, Torque, Radar, Accelerometers, Proximity) and Region - Growth, Trends, and Forecast (2019 - 2024)”, https://www.credenceresearch.com/report/aircraft-sensors-market, 2018, last access 24/03/2019.

[10] Bertagnoli G, Malavisi M, Mancini G. Large scale monitoring system for existing structures and infrastructures. In: IOP Conference Series Materials Science and Engineering 2019; 603(5), p. 052042. IOP Publishing.

[11] Ostachowicz W, Soman R, Malinowski P. Optimization of sensor placement for structural health monitoring: A review. Structural Health Monitoring 2019; 18(3): 963–88.

[12] Bartoli G, Betti M, Giordano S. In situ static and dynamic investigations on the ‘torre grossa’ masonry tower. Engineering Structures 2013; 52: 718–33.

[13] Ubertini F, Comanducci G, Cavalagli N. Vibration-based structural health monitoring of a historic bell-tower using output-only measurements and multivariate statistical analysis. Structural Health Monitoring 2016; 15: 438–57.

[14] Blanco, H., Boffill, Y., Lombillo, I., & Villegas, L. A new device for stress monitoring of ancient masonry buildings: Pilot study and results. Structural Control and Health Monitoring 2018; 25(8), e2197.

[15] Boffill, Y., Blanco, H., Lombillo, I., & Villegas, L. Device for continuous assessment of uniaxial stress of existing masonry structures: Laboratory validation. Structural Control and Health Monitoring 2019; 26(5), e2344.

[16] Bertagnoli G (inventor). Safecertifiedstructures Tecnologia (Assignee). Method and investigation device for measuring stresses in an agglomerate structure, Patent No. WO2017/178985 A1, 2016.

[17] Abbasi M, Bertagnoli G, Caltabiano D, Guidetti E (inventors). ST Microelectronics s.r.l. (Assegnee). Stress sensor for monitoring the health state of fabricated structures such as constructions, buildings, infrastructures and the like, Patent No. EP 3 392 637 B1, 2017.

[18] Anerdi C, Gino D, Malavisi M, Bertagnoli G. A sensor for embedded stress measure of concrete: Testing and material heterogeneity issues. In: Lecture Notes in Civil Engineering, 2020, ISBN: 978-3-030-23747-9.

[19] Abbasi M, Anerdi C, Bertagnoli G. An embedded stress measure of concrete: A new sensor able to overcome rheology issues. Proc, Italian Concrete Days 2020, Naples, April 2021.

[20] Pappalardo F, Pennisi A, Guidetti E, Doriani A (inventors). Capacitive pressure sensor for monitoring construction structures, particularly made of concrete, Patent n. US2019/0011320 A1, 2019.

[21] EN 1926. Natural stone test methods – determination of uniaxial compressive strength, 2006.

[22] EN 772-1. Method of test for masonry units – Part 1: Determination of compressive strength, 2011.

[23] EN 1015-11. Methods of test for mortar for masonry – Part 11:determination of flexural and compressive strength of hardened mortar, 2019.

[24] Italian Building Code. D.M. 17.01.2018 – Nuove Norme Tecniche per le Costruzioni, Italian Ministry for Infrastructure and Transportation, Rome, 2018.

[25] Italian Building Code Commentary. Circolare n.7 del 21.01.2019 – Istruzioni per l'applicazione dell'aggiornamento delle Norme tecniche per le costruzioni di cui al decreto ministeriale 17 gennaio 2018, Italian Ministry for Infrastructure and Transportation, Rome, 2019.

[26] Parisi F, Sabella G, Augenti N. Constitutive model selection for unreinforced masonry cross sections based on best-fit analytical moment-curvature diagrams. Engineering Structures 2016; 111: 451–66.

[27] Sargin M. Stress–strain relationship for concrete and analysis of structural concrete sections. In: Cohn MZ, editor. Study N.4, Solid Mechanics Division. Waterloo (Ontario): University of Waterloo; 1971.

[28] La Mendola L, Papia M. General stress–strain model for concrete or masonry response under uniaxial cyclic compression. Structural Engineering and Mechanics Journal 2002; 14(4): 435–54.

[29] Cavaleri L, Failla A, La Mendola L, Papia M. Experimental and analytical response of masonry elements under eccentric vertical loads. Engineering Structures 2005; 27(8): 1175–84.

[30] Benesty J, Chen J, Huang Y, Cohen I. Pearson correlation coefficient. In: Noise reduction in speech processing. Berlin: Springer, Heidelberg; 2009, p. 1–4.

[31] Pearson K. Notes on regression and inheritance in the case of two parents. Proceedings of the Royal Society of London 1895; 58: 240–2.

[32] Stigler, SM. Francis Galton's account of the invention of correlation. Statistical Science 1989; 4(2): 73–9.

[33] Patro S, Sahu KK. Normalization: A preprocessing stage. arXiv preprint 2015; arXiv:1503.06462.